Materials Horizons

Role of aggregates and microstructure of mixed-ionic-electronic-conductors on charge transport in electrochemical transistors

Journal:	*Materials Horizons*
Manuscript ID	MH-COM-01-2023-000017.R2
Article Type:	Communication
Date Submitted by the Author:	10-Apr-2023

Complete List of Authors:	LeCroy, Garrett; Stanford University, Department of Material Science and Engineering Cendra, Camila; Stanford University, Department of Material Science and Engineering Quill, Tyler; Stanford University, Department of Material Science and Engineering Moser, Maximilian; Oxford University Hallani, Rawad; King Abdullah University of Science and Technology, Solar and photovoltaics engineering research center Ponder, James; Air Force Research Laboratory Stone, Kevin; SLAC National Accelerator Laboratory, SSRL Kang, Stephen; Stanford University, Material Science and Engineering Liang, Allen; Stanford University, Department of Chemistry Thiburce, Quentin; Stanford University, Department of Material Science and Engineering McCulloch, Iain; Oxford University; King Abdullah University of Science and Technology Spano, Frank; Temple University Giovannitti, Alexander; Stanford University, Department of Material Science and Engineering Salleo, Alberto; Stanford University, Department of Materials Science and Engineering

New concepts statement

Our work provides insight into the operating mechanism of polymeric organic-mixed-ionic-electronic conductors (OMIECs) for electrochemical transistors (ECTs). By combining electrochemical and spectroelectrochemical measurements alongside electrochemical X-ray diffraction measurements, we demonstrate that holes and anions are placed in ordered polymer aggregates and crystallites at low charge carrier densities ($< 2x10^{20}$ cm^{-3}), giving rise to high device performance (transconductance and stability). Our results demonstrate that electrochemical charging of polymer thin films induces structural order along the polymer backbones. We interpret this structural ordering, where results suggest that polymer chains can form charge-transporting percolating networks, as the key factor for achieving high transconductance. Surprisingly, these dynamic rearrangements are highly reversible, but this reversibility only holds when high charge carrier densities are avoided. These findings challenge the current strategy for improving the performance of ECTs that focuses on designing OMIECs with high volumetric capacitance and high charge carrier mobility. Our results suggest that operating devices at high charge carrier densities results in the degradation of structurally-ordered aggregates, explaining operational device instabilities. We suggest that material chemistry should target OMIECs with a large number of electrochemical accessible aggregates, which form percolating networks at relatively low charge carrier densities where microstructural dynamics are largely reversible.

Journal Name

ARTICLE TYPE

Cite this: DOI: 00.0000/xxxxxxxxxx

Role of aggregates and microstructure of mixed-ionic-electronic-conductors on charge transport in electrochemical transistors†

Garrett LeCroy,[a‡] Camila Cendra,[a‡] Tyler J. Quill,[a] Maximilian Moser,[b] Rawad Hallani,[c] James F. Ponder Jr.,[d] Kevin Stone,[e] Stephen D. Kang,[a] Allen Yu-Lun Liang,[f] Quentin Thiburce,[a] Iain McCulloch,[b,c] Frank C. Spano,[g] Alexander Giovannitti,[*a,h] and Alberto Salleo[*a]

Received Date
Accepted Date

DOI: 00.0000/xxxxxxxxxx

Synthetic efforts have delivered a library of organic mixed-ionic-electronic conductors (OMIECs) with high performance in electrochemical transistors. The most promising materials are redox-active conjugated polymers with hydrophilic side chains that reach high transconductances in aqueous electrolytes due to volumetric electrochemical charging. Current approaches to improve transconductance and device stability focus mostly on materials chemistry including backbone and side chain design. However, other parameters such as the initial microstructure and microstructural rearrangements during electrochemical charging are equally important and are influenced by backbone and side chain chemistry. In this study, we employ a polymer system to investigate the fundamental electrochemical charging mechanisms of OMIECs. We couple in-situ electronic charge transport measurements and spectroelectrochemistry with ex-situ X-ray scattering electrochemical charging experiments and find that polymer chains planarize during electrochemical charging. Our work shows that the most effective conductivity modulation is related to electrochemical accessibility of well-ordered, interconnected aggregates that host high mobility electronic charge carriers. Electrochemical stress cycling induces microstructural changes, but we find that these aggregates can largely maintain order, providing insights on the structural stability and reversibility of electrochemical charging in these systems. This work shows the importance of material design for creating OMIECs that undergo structural rearrangements to accommodate ions and electronic charge carriers during which percolating networks are formed for efficient electronic charge transport.

1 Introduction

Redox-active conjugated polymers with polar side chains are a promising class of materials for electrochemical devices such

[a] Department of Materials Science and Engineering, Stanford University, Stanford, CA 94305, United States
[b] Department of Chemistry, Oxford University, Oxford, OX1 3TA, United Kingdom
[c] King Abdullah University of Science and Technology (KAUST), KAUST Solar Center, Thuwal, 23955-6900, Saudi Arabia
[d] Materials and Manufacturing Directorate, Air Force Research Laboratory, Wright-Patterson AFB, Ohio 45433, United States; UES, Inc., Dayton, Ohio 45432, United States
[e] Stanford Synchrotron Radiation Lightsource, SLAC National Accelerator Laboratory, Menlo Park, California 94025, United States
[f] Department of Chemistry, Stanford University, Stanford, CA 94305, United States
[g] Department of Chemistry, Temple University, Philadelphia, Pennsylvania 19122, United States
[h] Department of Chemistry and Chemical Engineering, Chalmers University of Technology, Gothenburg, 412 96, Sweden
‡ These authors contributed equally to the work
* alexander.giovannitti@chalmers.se; asalleo@stanford.edu

† Electronic Supplementary Information (ESI) available: Details on the polymer characterization, UV-Vis spectroscopy, spectroelectrochemistry, vibronic modeling, ex-situ charging GIWAXS measurements and measurements are provided in the supporting information]. See DOI: 00.0000/00000000.

as organic electrochemical transistors (OECTs), polymer batteries, chemical sensors, and synapses for neuromorphic computing[1–4]. In these devices, the key material functionality is electrochemical volumetric charging, where electronic charges are injected/collected at an electrode and transported through a π-conjugated system within the bulk of the material, while ions from the electrolyte stabilize electronic charges[5]. Given this interaction, the molecular design of conjugated polymer backbones and side chains profoundly affects material performance in electrochemical devices[6,7].

Recent advances in OMIECs, including controlling energy levels (polymer backbone engineering) and attaching side chains known to support ion transport (side chain engineering), have enabled OECTs with high transconductances and stable operation in aqueous electrolytes[8–18]. Backbone engineering has enabled tuning of the apparent redox-potentials and, consequently, operational voltages in electrochemical devices[8,11]. Similarly, side chain engineering, such as attaching ethylene glycol side chains, enhances solution processability, enables electrolyte and solvent molecules to swell the material bulk, and improves ion mobility[7,14].

Material nano-scale and microstructure are important factors for efficient electronic charge transport in organic semiconductors. However, complex structural rearrangements occur in OMIECs during electrochemical charging and discharging, and these structural dynamics have not yet been fully explored. Evidence for dynamic rearrangements in OMIECs have been observed during operando x-ray scattering experiments that show structural ordering of π-stacked chains in ionic-liquid gated OMIECS upon electrochemical charging[19]. Additionally, in-situ resonance Raman spectroscopy studies of poly(3-hexylthiophene-2,5-diyl) (P3HT) and 3,4-Propylenedioxythiophene (ProDOT) strongly suggest that backbone planarization occurs during electrochemical charging due to the presence of hole polarons along polymer backbones[20,21].

Moreover, several studies highlight that exposure of OMIECs to aqueous electrolytes and electrochemical charging produce volumetric swelling from ion and water penetration[2,14–16,22–24]. Recent ex-situ and in-situ electrochemical X-ray scattering experiments of OMIECs further demonstrated that this bulk volumetric swelling coincides with crystalline lamellar expansion, suggesting water and ions penetrate crystallites and facilitate electronic charge placement in structurally ordered regions[9,10,22,25–27]. Currently, chemical design guidelines that can yield OMIECs with suitable electronic and ionic charge transport combined with reversible electrochemical charging remain largely unknown. Thus, identifying chemical motifs for OMIECs that enable ionic and electronic charge placement with the formation of percolating charge-transporting networks during electrochemical cycling will enable rapid progress towards developing next-generation OMIECs.

In this work, we take advantage of two homopolymers with hydrophilic side chains specifically selected to assess the role of aggregates and microstructure of OMIECs on electrochemical charge transport properties. We vary the length of polymer side chains to influence microstructural order, while avoiding apparent changes of the chemical and physical properties of the polymers (i.e., comparable backbone electron density of the repeat unit, monomer-to-monomer torsional angle, and steric interactions). We find that optimal electrochemical device performance is found in OMIECs that allow for sufficient ion intercalation into ordered aggregates accompanied by the uptake of water molecules (swelling) during cycling. Our findings suggest that hole transporting OMIECs undergo backbone planarization where polymer chains can structurally order upon electrochemical charging. We suggest that polymer swelling plays an important role in creating the structural degrees of freedom for polymer chains to rearrange and accommodate counterions with minimal microstructural disruption, enabling the formation of percolating networks for efficient electronic charge transport.

2 Experimental

2.1 Synthesis

Polymer p(g3T2) and p(g2T2) were synthesized following procedures previously reported[2,16]. ^{1}H Nuclear magnetic resonance (NMR) spectra for p(g2T2) and p(g3T2) are shown in Figures S2 and S3, respectively.

2.2 Sample preparation

The polymers were dissolved in chloroform and stirred at 60 °C for 1 h, followed by filtering the solution (at room temperature) using a glass fiber filter (0.45 μm). Polymer thin films for electrochemical and spectroelectrochemical measurements were prepared on ITO substrates, bare Si substrates, or Si substrates with patterned gold contacts (i.e. OECT substrates) by spin coating polymer solutions of p(g2T2) and p(g3T2) at 1000 RPM for 60 s (5 mg mL^{-1} for OECT and ITO substrates, 10 mg mL^{-1} for Si substrates).

2.3 Spectroelectrochemical Measurements

A home-built setup was employed to conduct UV-Vis absorption measurements using an Ocean Optics light source (Tungsten Halogen Light Sources) and detector (QEPro, Ocean Optics, 200 μm slit width, cooled to -25 °C), as previously reported[2]. A quartz cuvette (20mm optical path length) was employed for spectroscopy measurements. An Ivium CompactStat potentiostat with an eDAQ leakless Ag/AgCl reference electrode and a Pt mesh counter electrode in Ar sat. 0.1 M NaCl aqueous electrolytes were employed for the electrochemical experiments. Optical absorption spectra were collected while performing cyclic voltamettry (CV) experiments where potentials were scanned from $\sim$0.1 V (at open circuit potential) to -0.5 V vs. Ag/AgCl and then followed by scans from -0.5 V vs. Ag/AgCl to 0.5 V vs Ag/AgCl at a scan rate of 50 mV s^{-1} where spectra were recorded every 100 ms. For spectroelectrochemistry data, averages of spectra collected over 50 mV steps were used to estimate the spectrum at a given potential vs. Ag/AgCl, representing the average of 10 individual spectra.

2.4 Optical absorption peak fitting

UV-Vis absorption spectra were fit with a model developed for general homopolymer aggregates[28]. Additional fitting details are provided in ESI† Sections S1.1 and S1.2.

2.5 OECT Measurements

We employed electrochemical transistors with channel dimensions of Width = 2 mm and Length = 50 and 100 μm. The patterning of the device was carried out by lift off with a parylene sacrificial layer[29,30]. The thickness of the spin cast devices was measured with a profilometer. OECTs were characterized with a bipotentiostat with two working electrodes (connected to the source and drain electrodes of the OECT), a counter electrode (Pt wire) and a reference electrode (leakless Ag/AgCl from eDAQ) using an Ar sat. 0.1 M NaCl aqueous solution. Details on this setup are provided in ESI† Section S1.6. Devices were operated with an offset of 10 mV (V_D = 10 mV) and always started at the potential from the open circuit voltage (OCV). The potential range of the measurements were -0.5 V to 0.3 V or -0.5 V to 0.5 V vs. Ag/AgCl with scan rate of 25, 50, 100 and 200 mV s^{-1} for five scans.

2.6 GIWAXS Measurements

Grazing incidence wide angle X-ray scattering (GIWAXS) was performed at the Stanford Synchrotron Radiation Lightsource (SSRL) on beam line 11-3. Samples were prepared on degenerately doped p^{++} silicon substrates with native oxide ($\rho \leq 0.005$ Ω-cm, Wafer Pro). Details of the beamline setup and data processing are provided in ESI† Section S1.3.

3 Results and discussion

3.1 Structural and electrochemical properties of a glycolated polythiophene system

We utilize two homopolymers based on a 3,3'-dialkoxybithiophene repeat unit (gXT2) with methyl end-capped diethylene (X=2, p(g2T2)) or triethylene glycol side chains (X=3, p(g3T2)), as depicted in Figure 1a[2,16]. These polymers are a useful model system to study structure-property relationships of OMIECs for electrochemical transistors, since they are homopolymers with symmetric repeat units that have a well-defined chemical structure. Data on matrix assisted laser desorption ionization time of flight (MALDI-ToF) and gel permeation chromatography (GPC) are presented in Figures S4-S6. The number average molecular weights (M_n) and dispersities (Đ) of the polymers as found from GPC in DMF are summarized in Table 1.

The polymer thin films spincoated from chloroform in this work are mildly oxidized at ambient conditions, so a reducing potential of –0.5 V vs. Ag/AgCl was applied to thin films in 0.1 M NaCl aqueous electrolyte to measure UV-Vis absorption spectra of neutral polymer films (Figure 1b, and Figure S7 for absorption spectrum of pristine, oxidized polymers). In its neutral state, polymer p(g3T2) displays two readily apparent vibronic transitions: the 0-0 and 0-1 transition peaks centered at 1.75 eV and 1.93 eV, respectively. The presence of resolvable vibronic features in p(g3T2) indicates increased aggregation relative to p(g2T2)[31].

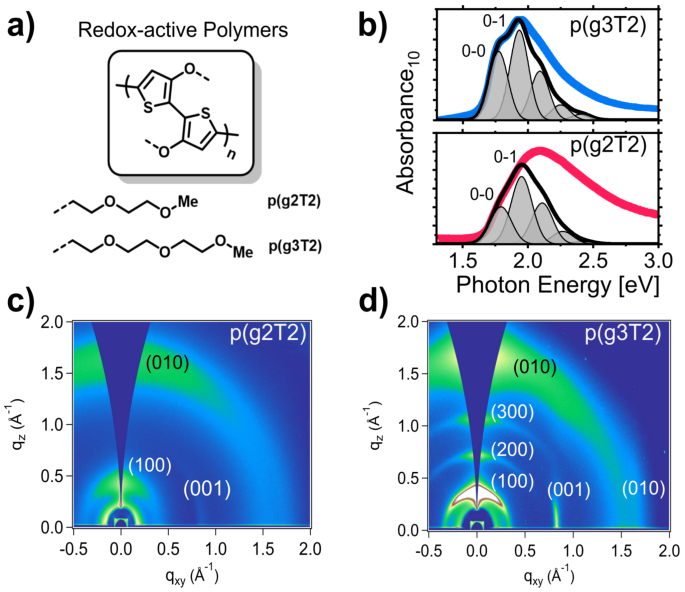

Fig. 1 A summary of structural and photophysical properties of p(g3T2) and p(g2T2). a) Molecular structure of the polymer p(g2T2) and p(g3T2). b) UV-Vis spectra of discharged, neutral polymer thin films with fits of a vibronic model for UV-Vis aggregate absorption as described in the main text. Fits are shown as solid lines, with individual vibronic fit components as shaded components. The 0-0 and 0-1 vibronic transitions are labelled. 2D GIWAXS patterns of as-cast films of c) p(g2T2) and d) p(g3T2).

Aggregate behavior results in a rich variety of photophysical features, and can arise from intermolecular and/or intramolecular interactions comprising as few as two chains, such as small domains with local, short-range order along the π-stack[32–34]. In this manuscript, we refer to "aggregates" as groups of interacting conjugated chromophores giving rise to known photophysical features[35–38].

An H-aggregate vibronic absorption model was used to measure aggregate fraction and interchain exciton coupling from solid-state absorption spectra of the homopolymers[28,35]. Details on the model fitting are shown in ESI† Sections S1.1 and S1.2. The photophysical aggregates probed with UV-Vis spectroscopy are distinct from crystallites, as they need not have long-range periodicity; consequently, crystallites contains aggregates but not all aggregates are in crystallites[31,39,40]. Exciton coupling is quantified by the interchain exciton bandwidth (W), with $W = 4J_{inter}$, where J_{inter} is the interchain exciton coupling. W acts a sensitive probe of material conjugation length, as W scales inversely with conjugation length[41]. That is, excitons that are more delocalized along a conjugated chain have a lower interchain bandwidth.

Fits of the neutral absorption spectra are presented in Figure 1b, and a summary of exciton bandwidth and film aggregate fraction are shown in Table 1. The exciton bandwidth in p(g3T2) ($\sim$ 74 meV) is comparable to values found in ordered regioregular P3HT thin films, while the bandwidth of p(g2T2) ($\sim$ 144 meV) is comparable to more disordered P3HT thin films spun from low boiling point solvents[37,42]. The estimated aggregate fractions, as found from the integrated model fits in Figure 1b, reveal that p(g3T2) contains more aggregates than p(g2T2) ($57 \pm 5\%$ and

Table 1 Properties of the polymers p(g2T2) and p(g3T2)

Polymer	M_n [kDa] / Đ	E_{Ox} [V vs Ag/AgCl]	W [meV]	Aggregate Amount [%]	Lamellar Spacing [nm] / Coherence Length [nm]
p(g2T2)	8.5 / 2.94	0.05	144 ± 3	32 ± 6	1.53 / 3.9
p(g3T2)	23.9 / 2.42	–0.20	74 ± 4	57 ± 5	1.73 / 13.2

$32 \pm 6\%$ respectively). Thus, not only does p(g3T2) have a higher degree of aggregation than p(g2T2), but these aggregates also exhibit a higher degree of intrachain order.

GIWAXS was used to investigate film microstructure. The X-ray scattering pattern of as-cast p(g2T2) in ambient conditions is composed of broad scattering peaks characteristic of polymers exhibiting weak intermolecular order (Figure 1c). In contrast, p(g3T2) exhibits a semicrystalline microstructure characterized by well-defined scattering peaks and streaks indicative of increased intermolecular ordering (Figure 1d). The coherence length (L_c) along the lamellar direction (h00) is shorter in p(g2T2) compared to p(g3T2) (3.9 nm or ∼2.5 lamellar planes compared to 13.2 nm or ∼7.6 lamellar planes) (Table 1). A peak in the Q_{xy} direction at ∼0.8 $Å^{-1}$ is observed in both polymers and attributed to ordering along the polymer backbone (001) planes (additional discussion in ESI† Section S1.8).

The two polymers presented in Figure 1 have different molecular weights. To determine that the observed structural properties are not purely a feature of molecular weight differences, a low molecular weight batch of p(g3T2) was synthesized (M_n = 10.3 kDa, PDI = 2.2, see ESI† Table S4). This low molecular weight polymer batch displays similar GIWAXS scattering patterns, CV behavior, and thin film absorbance to the higher molecular weight fraction (see ESI† Section 2.8). In this manuscript, we focused on the higher molecular weight fraction of p(g3T2), as the high molecular weight batch is more representative of most state-of-the-art OMIEC materials. Nevertheless the remarkable similarity of structural and photophysical properties of p(g3T2) between the two molecular weight fractions highlights the stark contrast between p(g3T2) and p(g2T2). Small alterations to side-chain length induce changes in the long-range ordering of the two materials, with the longer side-chains of p(g3T2) producing a more ordered, aggregated microstructure.

3.2 Electronic transport measurements

Due to the stark differences in structural and photophysical properties between p(g3T2) and p(g2T2), despite similar material chemistry, we identified this system as a useful set of materials for investigating the impact of microstructure and aggregate formation on the characteristics of electrochemical charging and charge transport properties, though we are careful to recognize that molecular weight has a profound effect on conductivity and carrier mobilities. We operate electrochemical transistors with p(g2T2) or p(g3T2) as the channel material and extract charge carrier density, n, while simultaneously measuring changes of the electronic conductivities, σ, as described in ESI† Section S1.6. Hole mobility, $\mu(E)$, as a function of charge carrier density is calculated using $\sigma(E) = n(E)\,\mu(E)\,e$, with the elemental charge, e, at applied potential, E, vs a Ag/AgCl reference electrode. The charge carrier density is calculated by integrating the current over the applied gate potential range, accounting for the scan rate, ν. CV measurements at various scan rates (25-200 mV s^{-1}) were performed to ensure that similar redox-states are accessible at increasing scan rate (ESI Figures S19 and S20).

To quantify charge carrier density during electronic charge transport measurements, we employ electrochemical transistors with defined channel geometries and apply a source-drain voltage of V_D = 10 mV. This allows us to limit parasitic electrochemical side-reactions. Figure 2a presents the cyclic voltammograms of the OECTs (channel dimensions of L = 100 μm and W = 2 mm) for p(g2T2) and p(g3T2) at a scan rate of 100 mV s^{-1}. Polymer p(g3T2) has two distinct redox-peaks ($E_{1/2}$[1] = -0.1 V and $E_{1/2}$[2] = 0.15 V vs. Ag/AgCl) and oxidizes at potentials more negative (a cathodic shift) in comparison to p(g2T2) which appears to have a broad oxidation peak ($E_{1/2}$ = 0.40 V vs. Ag/AgCl). The cathodic shift of p(g3T2) oxidation relative to p(g2T2) is consistent in the low molecular weight p(g3T2) (ESI S28), highlighting the redox behavior in these materials are strongly dependent on side-chain design. Charge carrier density as a function of potential (vs. Ag/AgCl) for both polymers is presented in Figure 2b. Figure 2c presents the relationship between the electronic conductivity and charge carrier density for p(g2T2) and p(g3T2) when cycling the polymer between -0.5 V to 0.5 V vs. Ag/AgCl. Figure 2d shows the associated changes in the differential hole mobility ($d\mu = \frac{1}{e}\frac{\partial\sigma}{\partial n}$) and thickness normalized transconductance ($g_m = \frac{L}{Wd}\frac{\partial I_D}{\partial V_G}$) for p(g2T2) and p(g3T2)[43,44]. Mobility estimates from a differential ($\frac{1}{e}\frac{\partial\sigma}{\partial n}$) approximate the contribution from incremental carriers near the Fermi-level accessed at each gate voltage, as opposed to the average mobility of all carriers, which is conventionally reported (ESI Figures S21 and S22).

Interestingly, the more ordered polymer, p(g3T2), has a conductivity turn-on at lower charge carrier density compared to p(g2T2) (Figure 2c). Moreover, the peak differential mobility for p(g3T2) (0.26 $cm^2V^{-1}s^{-1}$), which is reached at ∼0.16 V vs. Ag/AgCl ($n \sim 2.4 \times 10^{20} cm^{-3}$), is more than one order of magnitude larger than values measured for p(g2T2) ∼0.009 $cm^2V^{-1}s^{-1}$ which is reached at 0.5 V vs. Ag/AgCl ($n \sim 5.9 \times 10^{20} cm^{-3}$, see ESI† Table S2). p(g2T2) does not quite reach its peak mobility in the applied voltage range, but applying potentials greater than 0.5 V vs. Ag/AgCl results in degradation of the polymer as shown in ESI† Figure S21. Carrier mobility in conjugated polymers is influenced by molecular weight[31,45,46]. Thus, the greater molecular weight of p(g3T2) relative to p(g2T2) should be considered a factor when comparing the magnitude of conductivity (and hence mobility) between the two materials. However, the differences in charge density at maximum conductivity and turn-on carrier density in these materials still provides insights. The OECT performance differences between p(g3T2) and p(g2T2) warrant fur-

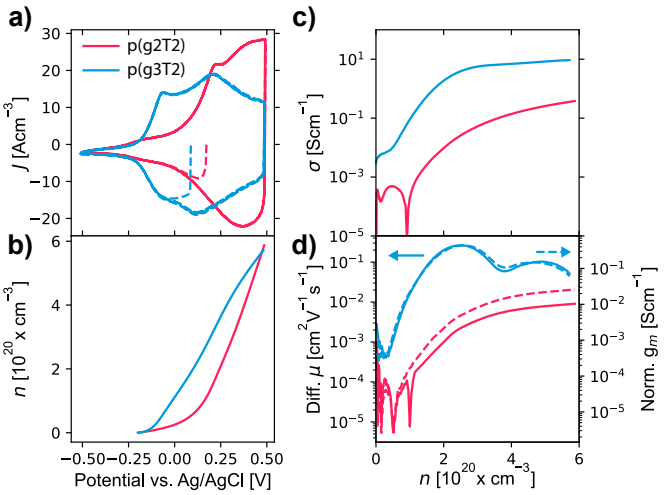

Fig. 2 OECT measurements of p(g2T2) and p(g3T2) in 0.1 M NaCl in Ar sat. solution, with V_D = 10 mV and a scan rate of 100 mV s^{-1}. a) Cyclic voltammogrammes of the polymers p(g2T2) and p(g3T2), showing 5 charging/ discharging cycles, b) Charge carrier density (n) with respect to potential vs. Ag/AgCl. c) Electronic conductivities and d) calculated differential mobilities ($d\mu$) (solid line) and thickness normalized transconductances (g_m) (dashed line) with respect to charge carrier density (n). The channel dimensions of the devices are Width = 2 mm, Length = 100 μm with thickness 199 nm for p(g2T2) and 149 nm for p(g3T2). Data for L = 50 μm is presented in the Supporting Information S18.

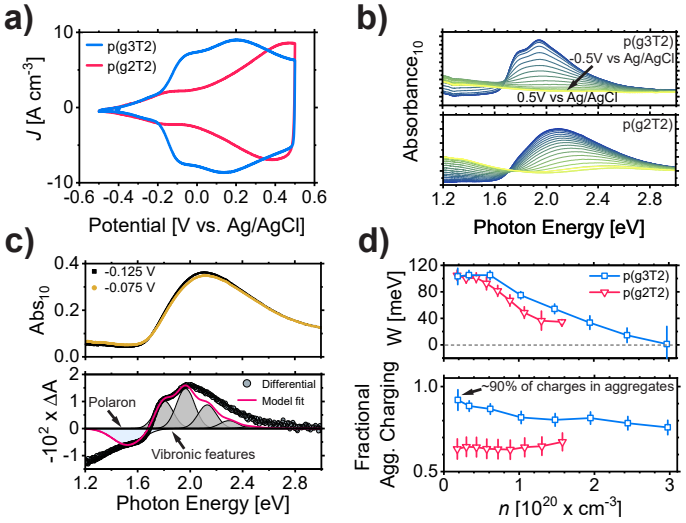

Fig. 3 Investigation of the photophysical properties during electrochemical charging of p(g2T2) and p(g3T2). a) CV measurements of polymer thin films between -0.5 V to 0.5 V vs. Ag/AgCl on ITO coated glass substrates with a scan rate of 5 mV s^{-1} in Ar sat. 0.1 M NaCl. b) Spectroelectrochemical measurements of p(g2T2) and p(g3T2), showing the changes of the absorption spectra during charging from -0.5 V to 0.5 V vs. Ag/AgCl (first charging cycle is shown) at a scan rate of 50 mV s^{-1}. Spectra shown represent average spectra over 50 mV steps. c) Two successive absorbance spectra from spectroelectochemistry of p(g2T2) at -0.125 V and -0.075 V vs Ag/AgCl are subtracted to yield a differential absorbance spectrum. A representative fit based on Equations S2 and S5 in the ESI† is shown, with vibronic and polaronic absorption features highlighted. d) Exciton bandwidth and the fraction of charges that go into aggregates (Fractional Agg. Charging) for differential absorbance data. Error bars represent propagated standard deviation from model fits.

ther investigation to unravel the role of role of aggregates and microstructure in charge transport.

3.3 Spectroelectrochemistry

To study aggregate features further, we use in-situ spectroelectrochemistry to correlate features of backbone and polaron optical absorption (e.g. polymer aggregate fraction and exciton bandwidth) to electronic charge density. Spectroelectrochemistry is performed on ITO coated glass substrates, so CV measurements were performed on these substrates to verify electrochemical behavior. CV measurements of polymer thin films on these substrates show a cathodic shift of the oxidation onset for p(g3T2) in comparison to (pg2T2) (Table 1, Figure 3a), in agreement with the transistor data (Figure 2a). Spectroelectrochemistry (Figure 3b) shows bleaching of polymer backbone vibronic transitions at photon energies above ~1.7 eV and an increase in polaronic absorption features at lower photon energies upon oxidation. Polaron absorption features in p(g3T2) decrease at potentials higher than 0.1 V vs. Ag/AgCl, (ESI Figure S9), consistent with reported formation of bipolaronic species at high charge carrier densities[47].

Spectroelectrochemistry yields further insight on the local structural order and location of charges (i.e. aggregate vs. amorphous regions) by looking at differential absorption, ΔA, where ΔA monitors features that are lost or gained during electrochemical charging. Differential absorption is particularly informative when stepping the potential in small increments, because it yields structural information about charges added at specific energies within the density of states and relates structural insights from optical absorption to carrier electronic transport properties. A representative example of these data for p(g2T2) is shown in Figure 3c. Fits for all potential steps are shown in ESI† Figures S10 and S11. Positive features in the differential spectra arise from the absorption of polaron/bipolaron charge carriers, and negative features in differential spectra arise from loss of vibronic absorption features (i.e. backbone bleaching) from neutral polymer chains that are becoming charged. Backbone bleaching features are well-fitted using the vibronic model developed by Spano, providing insights on the effective conjugation length and amount of aggregates charged at each charge carrier density following the same spectral analysis as described in Section 3.1. Additional details on this analysis are given in ESI† S1.2. We note that this differential data uncovers pronounced vibronic features that are masked in the standard Absorbance$_{10}$ measurements. Thus, the differential measurement reveals the presence of ordered aggregates in p(g2T2) that had gone undetected in conventional UV-Vis spectroscopy. These "hidden" ordered aggregates in p(g2T2) are indeed a feature of the material and not a molecular weight effect, because the pronounced vibronic features in the differential data of low molecular weight p(g3T2) are not masked in its standard Absorbance$_{10}$ data (ESI S29).

Despite the microstructural differences shown in Figure 1, exciton bandwidth of charged aggregates in both systems decreases

with increasing charge density, and reaches remarkably similar values in both materials studied at comparable charge densities. This suggests charges in both materials are being added to similarly ordered polymer aggregates with increasingly more intrachain order. Furthermore, molecular weight of p(g3T2) does not impact this observation, as the low molecular weight fraction displays a similar trend in bandwidth scaling with charge density (ESI S32). In p(g3T2), this bandwidth decrease coincides with a sharp increase in film conductivity (Figure 2). The bandwidth in p(g3T2) approaches ∼3 meV at higher carrier densities. This exceptionally low interchain exciton bandwidth is indicative of relatively long conjugated units with small interchain exciton delocalization. Though the exact bandwidth values depend on certain fit parameter choices (such as the Huang-Rhys factor), the trends observed in this work are robust to these choices (ESI Section 1.2)[34]. Analogous behavior has been observed in P3HT electrochemically doped with organic electrolytes, and, in these systems, this can represent subtle structural adjustments and charging of tie-chain regions between crystallites[48,49]. However, the glycolated materials in this study are not exact analogues of P3HT, as they have different backbone chemistry and swell significantly in aqueous electrolytes and represent more structurally dynamic materials with electrochemical charging[16,21,26]. That is, we leave open the idea that there could be significant structural rearrangement and even ordering in these swollen systems on electrochemical charging where charges remain in crystallites undergoing dynamic structural ordering. Indeed, it would be expected from energetic arguments that charges would occupy regions with the longest conjugation length available upon charge injection, so the evidence of charges occupying increasingly longer conjugation segments could indicate that these segments are forming upon doping as has been observed with ionic-liquid gated materials[19]. This is also in line with spectroscopic studies on other electrochemically doped materials that show evidence of backbone planarization upon electrochemical charging[20,21].

In p(g2T2), vibronic features in the differential spectra are not resolvable at $n > 1.6 \times 10^{20}\text{cm}^{-3}$, but the comparison of differential spectra with p(g3T2) at lower carrier densities provides insight on carrier mobility differences shown in Figure 2d, where, at carrier densities less than 10^{20}cm^{-3}, p(g2T2) has little increase in film conductivity with carrier density. Surprisingly, the exciton bandwidths of charged aggregates in this carrier density regime are similar to and even lower than that of p(g3T2), meaning that electrochemically accessible aggregates in p(g2T2) actually possess comparable intrachain order to those in p(g3T2). Therefore, the "quality" of aggregates does not explain the delayed onset of conductivity increase in p(g2T2) as might be expected from neutral absorbance spectra (Figure 1c). Rather, the amount of charges that are occupying aggregates in p(g2T2) is lower than that for p(g3T2) at comparable carrier densities. This suggests a sizable amount (∼40%) of injected charges in p(g2T2) are going to disordered, amorphous regions of the material, and potentially contributing little to overall film conductivity. If charges need to form a percolating network for high film conductivity, this observation of reduced aggregate charging in p(g2T2) may offer an explanation for its delayed conductivity onset relative to p(g3T2)

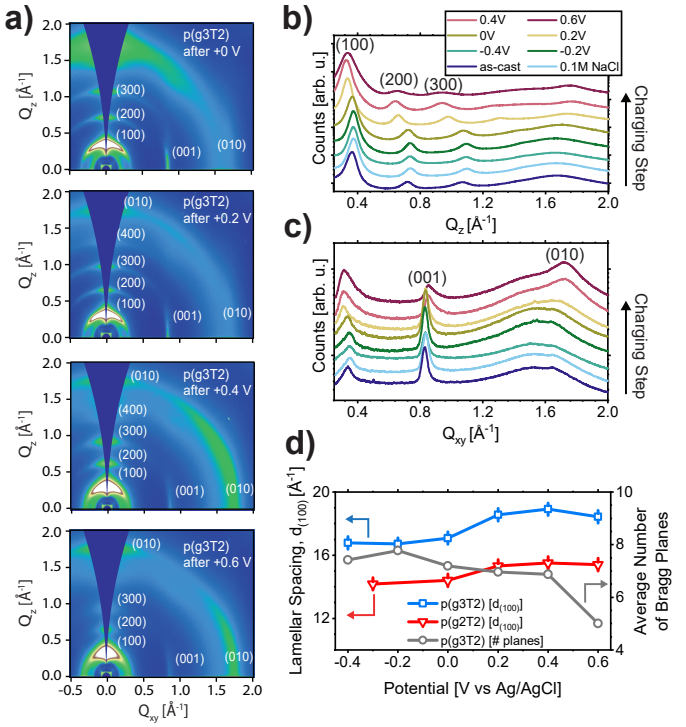

Fig. 4 Ex-situ electrochemical GIWAXS measurements of p(g2T2) and p(g3T2). a) 2D GIWAXS patterns of a p(g3T2) film measured after applying the indicated potential vs. Ag/AgCl (ex-situ charging) in Ar sat. aqueous electrolyte. Extended views of the b) out-of-plane (Q_z) X-ray scattering lineouts for the (100) and (200) lamellar stacking peaks and c) in-plane (Q_{xy}) X-ray scattering lineouts of a film of p(g3T2) charged to various potentials. Lineouts have been vertically offset to accentuate the peak shifts. d) Predominant lamellar lattice spacings of p(g3T2) and p(g2T2) and estimated average number of Bragg planes along the lamellar direction of p(g3T2). The lattice spacings and average number of Bragg planes are extracted from fitting the diffraction peaks. Error bars correspond to propagated standard deviation from peak fitting.

(Figure 2C).

3.4 Ex-situ GIWAXS

While spectroelectrochemistry yields insights on charge carrier occupation of short-range aggregates, differences in charge transport properties observed in Figure 2 also strongly depend on microstructure of the polymers. To probe microstructure, we conducted ex-situ charging GIWAXS experiments (Figure 4), carrying out amperometric charging measurements between -0.4 V to 0.6 V vs. Ag/AgCl with step size of 0.2 V (ESI Figure S16 for p(g2T2) and Figure S17 for p(g3T2)). GIWAXS is a direct probe of microstructural changes of crystalline regions (long-range order) and complements aggregate analysis found from spectroelectochemistry (short-range order). During the charging of thin films of p(g2T2) and p(g3T2), we observe a shift in the peak center position of the lamellar (h00) stacking peaks to lower q-values, indicating an increase in the lamellar spacing (Figure 4b and ESI† Figures S24 to S26). This lamellar expansion is attributed to intercalation of ions and solvent molecules in side chain regions of the crystallites[10,22,25,49–53]. While we attempted to fabricate devices with comparable charge injection properties during electro-

chemical measurements to allow for a direct comparison with the in-situ measurements, we observed a noticeable shift between oxidation potential on substrates for ex-situ GIWAXS measurements (p^{++}-doped silicon with native oxide) compared to those used for OECT and spectroelectrochemical measurements (Au or ITO). Observed differences in charge retention as well as shape of the cyclic voltammogram are also linked to changes of the substrate (see ESI† Figures S14 and S15 for comparison).

We attempt to quantify the structural disorder in polymer crystallites by estimating changes in the average number of lamellar Bragg planes that contribute to scattering peaks (i.e., coherence length divided by lattice spacing). Coherence length is based on peak breadth, Δq(h00) vs. diffraction order, h^2, analysis (see ESI† Section S1.8 for full details) of the lamellar peaks of p(g3T2) [54–56]. After charging the polymer to potentials above 0 V vs. Ag/AgCl, we observe a decrease in the average number of lattice Bragg planes and increased disorder along the lamellar direction (Figure 4d). We also note that in p(g3T2) the π-stacking peak becomes more prominent upon charging, signifying increased order in this crystallographic direction (see the (010) peak label in Figure 4b). Interestingly, at potentials greater than 0.2 V vs. Ag/AgCl, the (001) backbone peak ($Q_{xy} \sim 0.8$ Å^{-1}) decreases in intensity, broadens, and develops an apparent shoulder at higher Q, signaling a disruption of chain-to-chain registry that gives rise to diffraction approximately along the backbone direction (ESI Figure S27). However, full interpretation of the backbone peak is difficult and remains outside the scope of this work as the polymer unit cell would need to be known in more detail to correctly interpret this peak. Though charge density cannot be reliably determined in these ex-situ GIWAXS measurements, it is reasonable to speculate that electronic charge-charge interactions, bipolaron formation, counter-ion insertion, or a combination of all these effects can lead to this disruption of chain-to-chain registry.

3.5 Stability of Crystallites to Electrochemical Charging

The combination of OECT transport measurements, spectroelectrochemistry, and ex-situ GIWAXS suggest structurally ordered microstructures that result in a large amount of redox-accessible aggregates are beneficial for OECT electronic charge transport. Thus, it is insightful for future materials design to probe the disruption of these ordered microstructures by electrochemical charging. We assess the stability and potential disruption of long-range crystalline order during repeated electrochemical cycling via ex-situ GIWAXS in p(g3T2). We examine these changes in p(g3T2), since this material initially displays considerable order with multiple orders of scattering peaks that allow us to track their evolution on electrochemical cycling (Figure 5). Williamson-Hall type disorder analysis (Figure 5c and ESI† Table S3) shows that lamellar coherence decreases with continuous cycling (13.4 nm to 9.0 nm), lamellar paracrystallinity increases (9.4 % to 11.4%), and integration of partial lamellar pole figures reveal that the relative degree of crystallinity, rDoC, decreases by about half. Thus, we find that subjecting the material to these large oxidizing potentials permanently disrupts crystallites (Figure 5 and ESI† Table S3), which also explains film conductivity and mobility decreases on cycling to 0.5 V vs. Ag/AgCl (ESI Figure S23). Remarkably, the lamellar peak position is consistent before and after electrochemical cycling, suggesting reversible lamellar expansion from repeated ion intercalation. The edge-on π-stacking (Q$\sim$1.7 Å^{-1}) also remains present after stress cycling. There is a shift in the backbone scattering peak to lower spacing with a simultaneous increase in peak asymmetry that suggests some rearrangement of the polymer unit cell with electrochemical cycling (ESI Figure S27 shows (001) peak spacing). The presence of this backbone scattering and π-stacking peaks after electrochemical cycling strongly suggests that some structural order within crystallites is maintained. However, increased OECT transfer curve hysteresis coupled with decreased electronic transport properties (ESI S21-23) at potentials exceeding 0.3V and 0.5V for p(g3T2) and p(g2T2) respectively signal that the structural disruptions observed in ex-situ GIWAXS may indeed be enough microstructural change to disrupt effective charge transporting pathways.

Though we observe disruption of long-range microstructural features with ex-situ GIWAXS, the interchain coupling and overall amount of shorter-range photophysical aggregates is also of interest to understand electronic charge transport. We use spectroelectrochemistry for both p(g2T2) and p(g3T2) to probe the stability of these aggregates on electrochemical cycling. Surprisingly, both materials have relatively stable spectral properties even after 50 electrochemical stress cycles to 0.5 V vs Ag/AgCl, suggesting that aggregate regions are relatively unperturbed with electrochemical cycling, despite the disruption to lamellar crystalline coherence observed from GIWAXS (Figure 5). This suggests that there is excellent resilience of shorter-range order that can lead to photophysical aggregates but that does not contribute to longer-range crystalline ordering.

3.6 Discussion of OMIEC electrochemical charging

This study of two redox-active conjugated polymers with identical backbones – yet significant differences in their degree of solid-state structural ordering and electrochemical device performance – provides a model system to study electrochemical charging mechanisms of polymeric OMIECs.

Monitoring structural changes in ordered regions of the polymers via ex-situ electrochemical charging GIWAXS measurements provides insights on stability and overall structural order of crystallites during charging. As ions intercalate into side chains to compensate for electronic charges, perturbations in the crystallites are unavoidable (Figures 4 and 5 for polymer p(g3T2)). However, the observed lamellar expansion during electrochemical oxidation for p(g3T2) is mostly reversible upon reduction, showing that structure in the crystallites can be maintained when anions and water molecules are shuttling into and out of crystallites. Electrochemical cycling causes minor disruption to the π-stacking (Q$\sim$1.7 Å^{-1}) and backbone (Q$\sim$0.8 Å^{-1}) peaks. Remarkably, the π-stacking peak in p(g3T2) becomes more prominent upon oxidation (Figure 4b), signaling stronger π-π interactions for the oxidized polymer chains (i.e. once occupied with hole polarons) and suggesting the presence of hole polarons, counterions, or both can

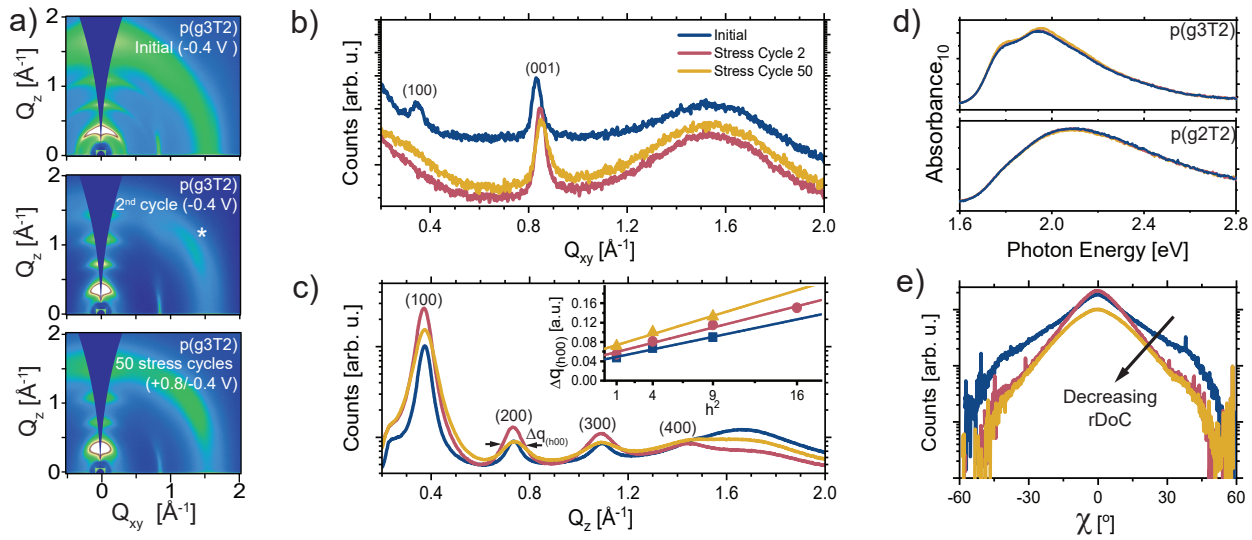

Fig. 5 Stability of the microstructure and photophysical properties of p(g3T2) a) ex-situ 2D GIWAXS patterns of p(g3T2) (top) initially discharged to -0.4V, (middle) discharged to -0.4 V after conducting the charging/discharging procedure outlined in Figure 4, and (bottom) discharged to -0.4 V after 50 charging/discharging cycles (charged between +0.8 V to -0.4 V vs Ag/AgCl). A peak of unconfirmed origin at Q ~1.5 Å^{-1} emerges (denoted as *).Note, the color scheme is the same for panels b), c), d), and e): Initially discharged (*Initial*, blue line), discharged after once charging discharging cycle (*Stress Cycle 2*, red line) and, discharged after 50 charging discharging cycles (*Stress Cycle 50*, yellow line)). b) X-ray scattering lineouts in the in-plane (Q_{xy}), and c) out-of-plane (Q_z) directions. Inset is Williamson-Hall type analysis with peak breadth (Δq(h00)) versus squared diffraction order (h^2) extracted from the lamellar stacking peaks after stress cycling and associated linear fits (solid lines). See Table S1 for full fitting results. d) $Absorbance_{10}$ of reduced polymer films (charged to -0.5 V vs Ag/AgCl) before and after electrochemical cycling under the same conditions used for ex-situ GIWAXS measurements. e) Lamellar (200) partial pole figures are shown. χ represents crystallite orientation relative to the substrate normal.

lead to some structural ordering of the material that is persistent on repeated electrochemical stress cycling.

Spectroelectrochemistry and fitting of vibronic bleaching features corroborate ex-situ GIWAXS measurements by demonstrating that most injected holes populate ordered H-aggregates in crystallites at relatively low charge carrier densities and also extends the insights by showing that holes occupy regions of increasing conjugation length (decreasing exciton bandwidth) as charge density increases, suggesting backbone planarization. Furthermore, these trends appear robust to molecular weight in this study (ESI Section S2.8). Charge placement (aggregate vs. amorphous regions) and aggregate quality (high vs. low exciton bandwidth) have remarkably similar scaling with charge density in p(g3T2) and p(g2T2), but the decrease in exciton bandwidth in p(g3T2) correlates to a steep increase in electronic mobility as seen in OECT transport measurements (Figure 2c). This highlights a key difference in the behavior in these two materials. While spectroelectrochemical measurements show that most charge carriers (greater than 60%) are added to aggregates in p(g2T2), significantly more charge carriers are added to aggregates in p(g3T2) that also have increasing effective conjugation length. The differences in charge population of aggregates can explain the delayed onset of conductivity in p(g2T2) compared to p(g3T2) (Figure 2), but the differences do not fully explain the carrier mobility of p(g2T2) compared with p(g3T2) at $n < 1.5 \times 10^{20}\text{cm}^{-3}$. Even taking an upper bound estimate of ~40% of injected charges in p(g2T2) as occupying disordered polymer regions (trap states) having no contribution to film conductivity, the order of magnitude lower carrier mobility in p(g2T2) shows that additional effects aside from charge placement in aggregate vs. amorphous regions must be lowering carrier mobility.

To rationalize this finding, we note the contrasting electronic and spectral behavior of p(g3T2) and p(g2T2). Holes added to p(g3T2) at lower carrier densities (until $n \sim 2.4 \times 10^{20}\text{cm}^{-3}$) have high mobility and mostly reside in ordered aggregates with large effective conjugation length (ESI Figure S13). In contrast, charge carriers added to p(g2T2) at lower carrier densities have several orders of magnitude lower mobility, but still mostly occupy aggregates with large effective conjugation length, meaning that charge placement in the two materials is similar. This suggests that the higher mobility in p(g3T2) arises from microstructural effects. Likely, the differences in mobility magnitude can be explained as molecular weight effects, with the higher molecular weight polymer having better connected aggregates. The overall higher amount of aggregates and crystallites in p(g3T2) allows charge transport paths through predominantly ordered regions, suggesting that such connectivity is the key to high mobility.

We link the swelling capability of polymers to their ability to change their microstructure upon electrochemical doping. We hypothesize that swelling is beneficial for rearrangement of polymer chains due to strong interactions between polymer chains and water molecules. Water molecules may act as plasticizers to support the reorganization of polymer chains upon hole and ion injection. The large difference between the swelling in aqueous electrolytes prior to and upon electrochemical charging (27 ± 10 and $245 \pm 21\%$ for p(g2T2) and p(g3T2) respectively when charged to 0.5 V vs Ag/AgCl) provides one explanation for why more holes and anions can be placed in aggregates of p(g3T2) in comparison to p(g2T2) (Figure 3)[16].

While polymer swelling may benefit ionic charge transport and

facilitate rearrangements of polymer chains that improve electronic charge transport (e.g. backbone planarization), uptake of solvent molecules and ions can also result in irreversible expansion of the lattice. This expansion can lead to disruption of electronic charge transport properties and may even lead to delamination or dissolution of the polymer film[57,58]. Consequently, p(g3T2) is more operationally stable in aqueous electrolyte OECTs when operated at low charge carrier densities up to $n \sim 3.5 \times 10^{20} \mathrm{cm}^{-3}$ where the amount of swelling is limited. When the device is operated at higher charge carrier densities, a drop in the electronic conductivity is observed and transconductance decreases irreversibly by approximately a factor of two (ESI Figure S23). Additionally, the differential mobility is observed to drop below the mean mobility in this carrier density regime, and we attribute this decrease in electronic mobility to decreasing structural order from solvent molecules and ion insertion in the polymer lattice (Figure 5) and possible structural effects of bipolaron formation at high charge carrier densities.

4 Conclusions

Our findings show that an ordered microstructure with a large fraction of aggregates is desirable for high transconductances in electrochemical transistors. Differences in charge occupation of aggregates between p(g3T2) and p(g2T2) can explain the differences in conductivity turn-on, but mobility and conductivity magnitude differences are linked to aggregate connectivity which depends on molecular weight. Remarkably though, electronic charges occupy similarly well-ordered aggregates in both materials studied, despite the large microstructural differences observed. We suggest that polymer chains can undergo planarization in the electrolyte-swollen state during electrochemical charging, consistent with other studies of electrochemically charged polymers[19–21]. Our study suggests that, provided aggregates are sufficiently interconnected, the combination of electronic carriers occupying aggregates and the proposed backbone planarization results in high hole mobilities.

Our analysis of the electrochemical stability further suggests that operating OMIECs at low charge carrier densities limits degradation of electronic charge transport properties in OECTs. More generally, our findings emphasize that side chain engineering has effects beyond facilitating solution processing and ion mobility. Side chain design has profound effects on microstructure which impacts both electronic transport and electrochemical charging processes. Future chemical design and device processing strategies of OMIECs should target conjugated polymers that form well-ordered microstructures with side chains that support reversible uptake of solvent molecules and ions during device operation in aqueous electrolytes. Furthermore, we argue that side chain and backbone design can not be easily deconvoluted and that understanding the subtle effects of side chain design on microstructure, aggregate properties, and electronic transport is necessary to rationalize materials design of next-generation OMIECs for electrochemical devices with high transconductance and operational stability.

Author Contributions

G.L. carried out spectroelectrochemical measurements and modeling of the absorption spectrum (under the supervision of F.C.S), C.C., T.Q., and K.S. and A.G. performed GIWAXS measurements, C.C. analyzed GIWAXS data,. Q.T. fabricated OECTs, A.G. and T.Q. carried out OECT measurements and A.G. and S.D.K. analyzed the data, M.M., R.H., and J.P. synthesized materials (under the supervision of I.M.), G.L., C.C., A.G., and A.S. wrote the manuscript. A.G. and A.S. oversaw the project.

Conflicts of interest

There are no conflicts to declare.

Acknowledgements

We thank Prof. Jenny Nelson, Nicholas Siemons, Christopher J. Takacs, and Kartik Choudhary for fruitful discussions. A.G. and A.S. acknowledge funding from the TomKat Center for Sustainable Energy at Stanford University and the National Science Foundation, Award DMR # 1808401. F.C.S. was supported by a grant from Department of Energy, DE-SC0020046. T.J.Q. and G.L. acknowledge support from the National Science Foundation Graduate Research Fellowship Program under grant DGE-1656518. Part of this work was performed at the Stanford Nano Shared Facilities (SNSF), supported by the National Science Foundation under award ECCS-1542152. Use of the Stanford Synchrotron Radiation Lightsource, SLAC National Accelerator Laboratory, is supported by the U.S. Department of Energy, Office of Science, Office of Basic Energy Sciences, under Contract No. DE-AC02-76SF00515. This material is based upon work supported by the U.S. Department of Energy, Office of Science, Office of Workforce Development for Teachers and Scientists, Office of Science Graduate Student Research (SCGSR) program. The SCGSR program is administered by the Oak Ridge Institute for Science and Education for the DOE under contract number DE-SC0014664.

Notes and references

1 J. Rivnay, S. Inal, A. Salleo, R. M. Owens, M. Berggren and G. G. Malliaras, *Nature Reviews Materials*, 2018, **3**, 17086.

2 D. Moia, A. Giovannitti, A. A. Szumska, I. P. Maria, E. Rezasoltani, M. Sachs, M. Schnurr, P. R. F. Barnes, I. McCulloch and J. Nelson, *Energy and Environmental Science*, 2019, **12**, 1349–1357.

3 O. Parlak, S. T. Keene, A. Marais, V. F. Curto and A. Salleo, *Sci Adv*, 2018, **4**,.

4 A. Melianas, T. J. Quill, G. LeCroy, Y. Tuchman, H. V. Loo, S. T. Keene, A. Giovannitti, H. R. Lee, I. P. Maria, I. McCulloch and A. Salleo, *Sci Adv*, 2020, **6**,.

5 B. D. Paulsen, K. Tybrandt, E. Stavrinidou and J. Rivnay, *Nature Materials*, 2020, **19**, 13–26.

6 I. F. Perepichka, M. Besbes, E. Levillain, M. Sallé and J. Roncali, *Chemistry of Materials*, 2002, **14**, 449–457.

7 J. Roncali, R. Garreau, D. Delabouglise, F. Garnier and M. Lemaire, *Journal of the Chemical Society-Chemical Communications*, 1989, 679–681.

8 C. B. Nielsen, A. Giovannitti, D.-T. Sbircea, E. Bandiello, M. R.

Niazi, D. A. Hanifi, M. Sessolo, A. Amassian, G. G. Malliaras, J. Rivnay and I. McCulloch, *Journal of the American Chemical Society*, 2016, **138**, 10252–10259.

9 L. Q. Flagg, C. G. Bischak, J. W. Onorato, R. B. Rashid, C. K. Luscombe and D. S. Ginger, *Journal of the American Chemical Society*, 2019, **141**, 4345–4354.

10 C. G. Bischak, L. Q. Flagg, K. Yan, T. Rehman, D. W. Davies, R. J. Quezada, J. W. Onorato, C. K. Luscombe, Y. Diao, C.-Z. Li and D. S. Ginger, *Journal of the American Chemical Society*, 2020, **142**, 7434–7442.

11 A. Giovannitti, R. B. Rashid, Q. Thiburce, B. D. Paulsen, C. Cendra, K. Thorley, D. Moia, J. T. Mefford, D. Hanifi, D. Weiyuan, M. Moser, A. Salleo, J. Nelson, I. McCulloch and J. Rivnay, *Advanced Materials*, 2020, **32**, 1908047.

12 A. Giovannitti, K. J. Thorley, C. B. Nielsen, J. Li, M. J. Donahue, G. G. Malliaras, J. Rivnay and I. McCulloch, *Advanced Functional Materials*, 2018, **28**, 1706325.

13 A. Giovannitti, C. B. Nielsen, D.-T. Sbircea, S. Inal, M. Donahue, M. R. Niazi, D. A. Hanifi, A. Amassian, G. G. Malliaras, J. Rivnay and I. McCulloch, *Nature Communications*, 2016, **7**, 13066.

14 A. Giovannitti, D.-T. Sbircea, S. Inal, C. B. Nielsen, E. Bandiello, D. A. Hanifi, M. Sessolo, G. G. Malliaras, I. McCulloch and J. Rivnay, *Proceedings of the National Academy of Sciences*, 2016, **113**, 12017–12022.

15 M. Moser, T. C. Hidalgo, J. Surgailis, J. Gladisch, S. Ghosh, R. Sheelamanthula, Q. Thiburce, A. Giovannitti, A. Salleo, N. Gasparini, A. Wadsworth, I. Zozoulenko, M. Berggren, E. Stavrinidou, S. Inal and I. McCulloch, *Advanced Materials*, 2020, **32**, 2002748.

16 M. Moser, J. Gladisch, S. Ghosh, T. C. Hidalgo, J. F. Ponder, R. Sheelamanthula, Q. Thiburce, N. Gasparini, A. Wadsworth, A. Salleo, S. Inal, M. Berggren, I. Zozoulenko, E. Stavrinidou and I. McCulloch, *Advanced Functional Materials*, 2021, **31**, 2100723.

17 A. Giovannitti, I. P. Maria, D. Hanifi, M. J. Donahue, D. Bryant, K. J. Barth, B. E. Makdah, A. Savva, D. Moia, M. Zetek, P. R. F. Barnes, O. G. Reid, S. Inal, G. Rumbles, G. G. Malliaras, J. Nelson, J. Rivnay and I. McCulloch, *Chemistry of Materials*, 2018, **30**, 2945–2953.

18 I. P. Maria, B. D. Paulsen, A. Savva, D. Ohayon, R. Wu, R. Hallani, A. Basu, W. Du, T. D. Anthopoulos, S. Inal, J. Rivnay, I. McCulloch and A. Giovannitti, *Advanced Functional Materials*, 2021, **31**, 2008718.

19 T. J. Quill, G. Lecroy, D. M. Halat, R. Sheelamanthula, A. Marks, L. S. Grundy, I. McCulloch, J. A. Reimer, N. P. Balsara, A. Giovannitti, A. Salleo and C. J. Takacs, *Nature Materials*, 2023.

20 J. Nightingale, J. Wade, D. Moia, J. Nelson and J.-S. Kim, *The Journal of Physical Chemistry C*, 2018, **122**, 29129–29140.

21 I. Bargigia, L. R. Savagian, A. M. Österholm, J. R. Reynolds and C. Silva, *Journal of the American Chemical Society*, 2021, **143**, 294–308.

22 A. Savva, C. Cendra, A. Giugni, B. Torre, J. Surgailis, D. Ohayon, A. Giovannitti, I. McCulloch, E. Di Fabrizio, A. Salleo, J. Rivnay and S. Inal, *Chemistry of Materials*, 2019, **31**, 927–937.

23 A. Savva, R. Hallani, C. Cendra, J. Surgailis, T. C. Hidalgo, S. Wustoni, R. Sheelamanthula, X. Chen, M. Kirkus, A. Giovannitti, A. Salleo, I. McCulloch and S. Inal, *Advanced Functional Materials*, 2020, **30**, 1907657.

24 J. Gladisch, E. Stavrinidou, S. Ghosh, A. Giovannitti, M. Moser, I. Zozoulenko, I. McCulloch and M. Berggren, *Advanced Science*, 2020, **7**, 1901144.

25 C. Cendra, A. Giovannitti, A. Savva, V. Venkatraman, I. McCulloch, A. Salleo, S. Inal and J. Rivnay, *Advanced Functional Materials*, 2019, **29**, 1807034.

26 B. D. Paulsen, R. Wu, C. J. Takacs, H. Steinrück, J. Strzalka, Q. Zhang, M. F. Toney and J. Rivnay, *Advanced Materials*, 2020, **32**, 2003404.

27 B. D. Paulsen, A. Giovannitti, R. Wu, J. Strzalka, Q. Zhang, J. Rivnay and C. J. Takacs, *Small*, 2021, **17**, e2103213.

28 F. C. Spano, *The Journal of Chemical Physics*, 2005, **122**, 234701.

29 D. Khodagholy, J. Rivnay, M. Sessolo, M. Gurfinkel, P. Leleux, L. H. Jimison, E. Stavrinidou, T. Herve, S. Sanaur, R. M. Owens and G. G. Malliaras, *Nature Communications*, 2013, **4**,.

30 M. Sessolo, D. Khodagholy, J. Rivnay, F. Maddalena, M. Gleyzes, E. Steidl, B. Buisson and G. G. Malliaras, *Advanced Materials*, 2013, **25**, 2135–2139.

31 R. Noriega, J. Rivnay, K. Vandewal, F. P. V. Koch, N. Stingelin, P. Smith, M. F. Toney and A. Salleo, *Nature Materials*, 2013, **12**, 1038–1044.

32 H. Yamagata and F. C. Spano, *The Journal of Chemical Physics*, 2012, **136**, 184901.

33 F. C. Spano and C. Silva, *Annual Review of Physical Chemistry*, 2014, **65**, 477–500.

34 N. J. Hestand and F. C. Spano, *Chemical Reviews*, 2018, **118**, 7069–7163.

35 F. C. Spano, *Chemical Physics*, 2006, **325**, 22–35.

36 D. T. Duong, M. F. Toney and A. Salleo, *Physical Review B*, 2012, **86**,.

37 J. Clark, J.-F. Chang, F. C. Spano, R. H. Friend and C. Silva, *Applied Physics Letters*, 2009, **94**, 163306.

38 J. Clark, C. Silva, R. H. Friend and F. C. Spano, *Physical Review Letters*, 2007, **98**,.

39 R. J. Kline and M. D. McGehee, *Journal of Macromolecular Science, Part C: Polymer Reviews*, 2006, **46**, 27–45.

40 G. Juška, K. Arlauskas, M. Viliūnas, K. Genevičius, R. Österbacka and H. Stubb, *Physical Review B*, 2000, **62**, R16235–R16238.

41 W. Barford, *The Journal of Chemical Physics*, 2007, **126**, 134905.

42 P. Pingel, A. Zen, R. D. Abellón, F. C. Grozema, L. D. A. Siebbeles and D. Neher, *Advanced Functional Materials*, 2010, **20**, 2286–2295.

43 B. D. Paulsen and C. D. Frisbie, *The Journal of Physical Chemistry C*, 2012, **116**, 3132–3141.

44 I. N. Hulea, H. B. Brom, A. J. Houtepen, D. Vanmaekelbergh, J. J. Kelly and E. A. Meulenkamp, *Physical Review Letters*, 2004, **93**,.

45 R. J. Kline, M. D. McGehee, E. N. Kadnikova, J. Liu and J. M. J. Fréchet, *Advanced Materials*, 2003, **15**, 1519–1522.

46 K. Gu, C. R. Snyder, J. Onorato, C. K. Luscombe, A. W. Bosse and Y.-L. Loo, *ACS Macro Letters*, 2018, **7**, 1333–1338.

47 C. Enengl, S. Enengl, S. Pluczyk, M. Havlicek, M. Lapkowski, H. Neugebauer and E. Ehrenfreund, *Chemphyschem*, 2016, **17**, 3836–3844.

48 J. K. Harris, B. Neelamraju and E. L. Ratcliff, *Chemistry of Materials*, 2019, **31**, 6870–6879.

49 E. M. Thomas, M. A. Brady, H. Nakayama, B. C. Popere, R. A. Segalman and M. L. Chabinyc, *Advanced Functional Materials*, 2018, **28**, 1803687.

50 J. O. Guardado and A. Salleo, *Advanced Functional Materials*, 2017, **27**, 1701791.

51 K. Tashiro, Y. Minagawa, M. Kobayashi, S. Morita, T. Kawai and K. Yoshino, *Japanese Journal of Applied Physics Part 2-Letters and Express Letters*, 1994, **33**, L1023–L1026.

52 T. Kawai, M. Nakazono, R.-I. Sugimoto and K. Yoshino, *Journal of the Physical Society of Japan*, 1992, **61**, 3400–3406.

53 T. Kawai, M. Nakazono and K. Yoshino, *Journal of Materials Chemistry*, 1992, **2**, 903.

54 L. H. Jimison, A. Salleo, M. L. Chabinyc, D. P. Bernstein and M. F. Toney, *Physical Review B*, 2008, **78**,.

55 J. Rivnay, S. C. B. Mannsfeld, C. E. Miller, A. Salleo and M. F. Toney, *Chemical Reviews*, 2012, **112**, 5488–5519.

56 T.-M. Wu, J. Blackwell and S. N. Chvalun, *Macromolecules*, 1995, **28**, 7349–7354.

57 J. Gladisch, E. Stavrinidou, S. Ghosh, A. Giovannitti, M. Moser, I. Zozoulenko, I. McCulloch and M. Berggren, *Advanced Science*, 2020, **7**, 1901144.

58 A. A. Szumska, I. P. Maria, L. Q. Flagg, A. Savva, J. Surgailis, B. D. Paulsen, D. Moia, X. Chen, S. Griggs, J. T. Mefford, R. B. Rashid, A. Marks, S. Inal, D. S. Ginger, A. Giovannitti and J. Nelson, *Journal of the American Chemical Society*, 2021, **143**, 14795–14805.